Unraveling the Improved ORR Activities in Pt/TiO₂/C hybrids: The Role of Pt Morphology and Reactive Surface Species

Eduardo C. M. Barbosa[a, +], Luanna S. Parreira[a, +], Isabel C. de Freitas[a], Luci R. Aveiro[b], Daniela C. de Oliveira[c], Mauro C. dos Santos[b], and Pedro H. C. Camargo[a,]*

[a] Departamento de Química Fundamental, Instituto de Química, Universidade de São Paulo, Av. Prof. Lineu Prestes, 748, 05508-000 São Paulo, SP, Brazil

[b] Laboratório de Eletroquímica e Materiais Nanostruturados - Centro de Ciências Naturais e Humanas, Universidade Federal do ABC, Rua Santa Adélia, 166, 09210-170, Santo André, SP, Brazil

[c] Centro Nacional de Pesquisa em Energia e Materiais, Laboratório Nacional de Luz Síncrotron, 13083-970, Campinas, SP, Brasil

*Corresponding author: Email: camargo@iq.usp.br

[+] These authors contributed equally to this article

Abstract

Further improvements and mechanistic understanding of the electrocatalytic enhancements towards the oxygen reduction reaction (ORR) are required to meet cost/energy demands and thus enable their practical applications in polymer electrolyte fuel cells. An investigation of the electrocatalytic enhancement mechanisms and stability of controlled electrocatalysts comprised Pt nanoparticles supported on TiO_2/C materials was herein performed. The catalysts were prepared by depositing Pt, over the surface of TiO_2 colloidal spheres. These materials were then supported onto Vulcan carbon to produce $Pt/TiO_2/C$. The effect of Pt coverage at the TiO_2 surface as well as the Pt/TiO_2 loading on carbon over their ORR activity and stability were investigated. Results indicate that the control over Pt coverage at the surface played a pivotal role on activity optimization, in which an association between Pt content at the TiO_2 surface and ORR activity was established. The ORR activity and stability were superior as compared to commercial Pt/C (E-TEK). Variations in catalytic activity could be correlated with the morphological features and with the concentration of surface reactive groups. Results described herein suggest that the understanding of the electrocatalytic enhancement mechanism together with the controlled synthesis of Pt-based nanomaterials may lead to tailored surface properties and thus ORR activities.

Keywords: Oxygen Reduction Reaction, Controlled Synthesis, Electrocatalysis, Pt, TiO_2.

Introduction

The oxygen reduction reaction (ORR) has been attracting a great deal of attention towards a sustainable future[1–10]. Due to its sluggish kinetics, this reaction requires the utilization of electrocatalysts and plays a central role at the cathode in proton exchange membrane (PEM) fuel cells, contributing to the energy production of these devices[11–15]. The most used electrocatalysts for the ORR in PEMs are based on platinum nanoparticles (Pt NPs) supported on high surface area materials[16–18]. Due to the high costs and low abundance of Pt, the reduction in Pt loading or even developing Pt-free electrocatalysts represents a very important challenge[19–22]. Recently, significant progress has been achieved in performance through the control over the Pt shape, size, composition (alloys and multimetallic systems), and structure (Pt-based nanostructures with hollow interiors)[16,23]. Nevertheless, further improvements and mechanistic understanding of the electrocatalytic enhancements towards the ORR are still required to meet cost/energy demands and thus enable the widespread application of these devices[3,24,25].

In addition to the control over the abovementioned NPs physical and chemical parameters, the optimization over metal-support interactions represents an interesting approach to maximize electrocatalytic performance. This effect has also been intensively investigated in nanocatalysis[26–30]. Regarding the ORR, most supports are comprised of conductive carbon nanomaterials[6,20,31]. However, carbon supports usually corrode to form carbon dioxide, leading to the collapse and agglomeration of Pt NPs and thus the loss of activity[11,26,32–34]. Therefore, the utilization of other supports is promising to improve both the

stability and performances. Among the several materials that show promise as a support, TiO_2 represents an important example[34–36]. In addition to its corrosion resistance, TiO_2 presents a low cost, is commercially available, and several protocols for the synthesis with controlled morphologies have been reported[37–42]. However, a major drawback is that, as TiO_2 is a semiconductor, its electrical conductivity must be enhanced to be used as a catalyst support material. In order to circumvent this problem, hybrid materials comprised of TiO_2 and carbon have been proposed as supports. Although this system combines the attractive features of both materials, a deeper mechanistic understanding of effect and role of this hybrid support over the electrocatalytic activities and stabilities is required[32,33,35,43,44].

In this paper, we performed an investigation of the electrocatalytic enhancement mechanisms and stability of Pt NPs supported on TiO_2/C materials. Specifically, our electrocatalyst was prepared by depositing Pt NPs over the surface of TiO_2 colloidal spheres (generating Pt/TiO_2 NPs), which were then supported over Vulcan carbon by wet impregnation to produce Pt/TiO_2/C NPs. We investigated the effect of the Pt NPs morphology and coverage at the TiO_2 surface as well as the Pt/TiO_2 loading on carbon over their ORR activity and stability. The performance was benchmarked against the commercial Pt/C (E-TEK) material. Our results indicated that the control over the Pt coverage at the surface played a pivotal role over the optimization of activities, in which a relationship between Pt content at the TiO_2 surface and ORR activity was established. The ORR activity and stability were superior as compared to commercial Pt/C (E-TEK). The variations in catalytic activity could be correlated with the morphological features as well as the concentration of surface reactive

groups, such as adsorbed oxygenated species. Moreover, as our material contains TiO_2, the electrocatalytic activity could be further enhanced by UV-excitation.

Experimental

Materials and Instrumentation: $H_2PtCl_6 \cdot 6H_2O$ (Chloroplatinic acid hexahydrate, Sigma-Aldrich), PVP (polyvinylpyrrolidone, Sigma-Aldrich, MW 55 000 g mol^{-1}), EG (ethylene glycol, 99.5%, Synth), C_3H_6O (acetone, 99.5%, Synth), $C_2H_4O_2$ (acetic acid, 99.7%, Vetec), $C_6H_8O_6$ (ascorbic acid, 99.0%, Sigma-Aldrich), Ti(OBu)$_4$ (titanium butoxide, 97%, Sigma-Aldrich), Vulcan XC-72 Carbon (Cabot®), H_2SO_4 (sulfuric acid, 70%, P.A. Synth), Nafion® (5 wt.%, Fluka), and Pt/C E-TEK 10 wt.% were used as received. All chemicals were analytical grade reagents and were used without further purification. Deionized water (18.2 MΩ) was used throughout the experiments.

Scanning electron microscopy (SEM) images were obtained using a JEOL microscope FEG-SEM JSM 6330F operated at 5 kV. The samples were prepared by drop-casting an aqueous suspension of the nanostructures on a Si wafer followed by drying under ambient conditions. Size distribution profile was determined by individually measuring the size of 200 particles from SEM images. Transmission electron microscopy (HRTEM) images were obtained using a Tecnai FEI G20 operated at 200 kV. Samples were prepared by drop casting an alcoholic suspension of each particle in a carbon-coated copper grid followed by drying under ambient conditions.

The X-ray photoelectron spectroscopy (XPS) analyses were performed using a SPECSLAB II (Phoibos-Hsa 3500 150, 9 channeltrons) SPECS spectrometer, with an Al Kα

source (E = 1486.6 eV) working at 12 kV, Epass = 40 eV, with 0.2 eV energy step. The synthesized electrocatalysts were kept on stainless steel sample-holders and transported under inert atmosphere into the pre-chamber of the XPS staying under vacuum for 2 hours. The residual pressure in the analysis chamber was of approximately 1×10^{-9} Torr. The binding energies (BE) of Pt 4f, Ti 2p, O 1s, and C 1s spectral peaks were adjusted using the C 1s peak as reference, placed at 284.5 eV, providing accuracy within ± 0.2 eV.

X-ray diffraction (XRD) data were obtained using a Rigaku - Miniflex equipment with CuKα radiation of 1.5406 Å and the diffraction patterns were acquired in the range of 2θ = 10 – 80° with a 1° min–1 scanning speed. Pt atomic percentages were measured by inductively coupled plasma optical emission spectrometry (ICP-OES) using a Spectro Arcos equipment at IQ-USP analytical center facilities. Samples were prepared by digesting them using aqua regia at reflux for 2 hours at 100°C. After digestion, samples were diluted using distilled water.

Synthesis of TiO$_2$ colloidal spheres: The synthesis followed a previously reported procedure.[45–47] Typically, Ti(OBu)$_4$ (4 mL) were added dropwise to ethylene glycol (90 mL) and kept under vigorous stirring at room temperature for 8 hours. This mixture was then quickly poured into a mixture containing acetone (400 mL), deionized water (5 mL), and acetic acid (2 mL). Subsequently, the mixture was kept under stirring at room temperature for 2 hours followed by aging for 3 more hours. At this stage, titanium glycolate microspheres were formed. They were washed and isolated by successive rounds of centrifugation, removal of the supernatant, and re-suspension in ethanol. In the next step, deionized water (50 mL) was added to the solid material comprising titanium glycolate microspheres, the materials were

re-suspended, and this mixture was kept under stirring at 70 °C for 8 hours to produce TiO2

colloidal spheres. This material was washed and isolated by successive rounds of

centrifugation, removal of the supernatant, and re-suspension with water and ethanol. The

TiO_2 colloidal spheres were then resuspended in deionized water (500 mL).

Synthesis of Pt/TiO$_2$ via Pt seeded growth: TiO$_2$ microspheres (12 mg) suspended in

deionized water (6 mL) were added to a mixture containing deionized water (12 mL), ascorbic

acid (12 mg), and PVP (70 mg). This orange mixture was kept under stirring for 10 minutes at

90 °C and at this point, $PtCl_6^{2-}{}_{(aq)}$ (6 mL, 3.0 mmol L^{-1}) was quickly added to the mixture, which

after 10 minutes produced a change in color to black as a result of Pt deposition at the TiO$_2$

surface. The reaction was allowed to proceed for other 30 minutes at 90°C. This was the first

reduction step, the material obtained at this stage was denoted Pt/TiO$_2$-1, in which the

number 1 refers to one Pt deposition step. A second reduction step was performed by adding

more $PtCl_6^{2-}{}_{(aq)}$ solution (6 mL, 3.0 mmol L^{-1}) to the reaction mixture obtained at the end of

the first reduction step, followed by stirring at 90°C for other 30 min. Similarly, a third

reduction step was carried out by adding more $PtCl_6^{2-}{}_{(aq)}$ solution (6 mL, 3.0 mmol L^{-1}) to the

reaction mixture obtained at the end of the second reduction step, followed by stirring at 90

°C for another 30 min. As described in the first deposition step, the solids that were obtained

after the second and third reduction steps were denoted Pt/TiO$_2$-2 and Pt/TiO$_2$-3,

respectively. These materials were isolated by stopping the reaction at the end of each

corresponding reduction step. In all cases, the products were harvested by centrifugation,

washed several times with water and ethanol, and re-suspended in water for further use. These samples were dried and weighed for ICP-OES analyses.

Impregnation of Pt/TiO$_2$-1, Pt/TiO$_2$-2, and Pt/TiO$_2$-3 onto carbon Vulcan XC-72: The Pt/TiO$_2$-1, Pt/TiO$_2$-2, and Pt/TiO$_2$-3 materials were impregnated onto a carbon support in order to produce 10% wt. Pt/TiO$_2$-1/C, Pt/TiO$_2$-2/C, and Pt/TiO$_2$-3/C on Vulcan XC-72 Carbon (Cabot®) by a wet impregnation method. Typically, Carbon (50 mg) was used as support for the nanomaterials. The supports were added to aqueous suspensions containing 5 mg of each material and left under vigorous magnetic stirring at 110°C until dry.

Electrochemical studies: The electrochemical experiments were performed at 25°C in an electrochemical three-electrode cell with H$_2$SO$_4$ (80 mL, 0.5 mol L^{-1}) as support electrolyte using a potentiostat/galvanostat PGSTAT model 302 N (Autolab®) coupled to a rotating ring-disk electrode accessory (Pine®) and controlled by the Nova 10.1 software. The counter electrode was a platinum rod, while an Ag/AgCl electrode (Analyzer®) was used as reference. The work electrode was a rotating ring-disk electrode consisting of a glassy carbon disk (0.2475 cm²) and platinum ring (0.1866 cm²) with the collection factor of 0.28. After thoroughly characterizing the catalysts, a suspension of each material was prepared in milli-Q water in order to deposit them onto the electrode. An ink was prepared using 1 mg of electrocatalyst and 1 mL of ultrapure water (Milli Q system, 18.2 mΩ cm^{-1}) sonicated for 30 minutes. The glassy carbon disk surface was covered by a drop of 20 uL of the electrocatalytic ink and dried under N$_2$ flux. Subsequently, 20 μL of a 1:100 solution of Nafion® and ultrapure

water were dropped onto the material, and then further dried under N_2 flux at room temperature. The electrocatalysts were then further characterized regarding their electrocatalytic properties.

For CO stripping measurements, carbon monoxide was adsorbed on a 20 mV polarized electrode, during 5 minutes, immersed in a H_2SO_4 solution (0.5 mol L^{-1}). Subsequently, CO was removed from the electrolyte by purging with N_2 for 25 minutes, and three consecutive cyclic voltammetries were run with a scan rate of 10 mV s^{-1} within the potential range of 0.01 to 1.01 V *versus* RHE reference electrode. The electrochemical surface areas (ESA)[48] for CO stripping were obtained by integrating the area under each CO oxidation peaks in the first voltammetric cycle (Q_{CO}, in mC), these were then divided by the charge needed to oxidize a CO monolayer adsorbed onto a Pt surface (Q_{CO} = 420 μC cm^{-2}). These values were then normalized by the mass of Pt on each electrode and the ECSA was obtained in m^2 g^{-1}.

For the oxygen reduction reaction (ORR), linear scanning voltammograms were collected with a scan rate of 0.01 V s^{-1} in an ultrapure O_2 saturated H_2SO_4 electrolyte (0.5 mol L^{-1}, 30 minutes of O_2 purge) in the potential range between 1.21 and 0.21 V (*vs* RHE) in different rotation speeds (ω) from 100 to 2500 rpm. For experiments performed under light irradiation, a UV LED stick (UVP Pen-Ray (R) Light source) was used. All the analyses were performed in triplicate.

Accelerated stress tests (AST): In order to study the stability of the electrocatalysts, the most promising catalyst (Pt/TiO₂-2/C) was compared to the commercial material (Pt/C E-

TEK) in accelerated stress tests. A typical test was performed in H_2SO_4 (0.5 mol L^{-1}) as support electrolyte. An ORR polarization curve was then collected with a scan rate of 0.01 V s^{-1} in an ultrapure O_2 saturated H_2SO_4 electrolyte (0.5 mol L^{-1}, 30 minutes of O_2 purge) in the potential range between 1.21 and 0.21 V (*vs* RHE) in different rotation speeds (ω) from 100 to 2500 rpm. After performing the ORR, the electrolyte was switched for a fresh one and N_2 was bubbled for 30 minutes before performing the cycles, 1000 cyclic voltammetries were run with a scan rate of 100 mV s^{-1} within the potential range of 0.01 to 1.01 V *versus* RHE. Oxygen was once again bubbled for 30 minutes and ORR was performed in the same conditions as previously established.

Results and discussion

Figure S1A and B show SEM and HRTEM images of the TiO_2 colloidal spheres that were employed as starting materials for the production of our hybrid electrocatalyst. The TiO_2 spheres displayed spherical shape and were 267.8 ± 37.8 nm in diameter. Although they appear to be smooth from SEM images, HRTEM results revealed that they are comprised of TiO_2 nanocrystallites (around 10 nm in size) and displayed rough surfaces. They were crystallized as anatase according to previously reported XRD and Raman data[45,49,50].

The TiO_2 colloidal spheres were then employed as seeds for Pt deposition at their surface with controllable sizes and coverage by a facile route based on sequential deposition steps as depicted in Figure S2[45]. This approach employed $PtCl_6^{2-}$ as the Pt precursor, ascorbic acid as a reducing agent, PVP as a stabilizer, water as the solvent, and 90 °C as the reaction temperature. We were interested in controlling the size and coverage of Pt at the surface by

performing successive deposition steps, and then understanding how these parameters affect the electrocatalytic activity of the generated materials towards the ORR. Specifically, three Pt deposition steps were performed, which led to Pt/TiO$_2$-1, Pt/TiO$_2$-2, and Pt/TiO$_2$-3 materials (obtained after one, two, and three Pt deposition steps, respectively).

SEM images for the Pt/TiO$_2$-1, Pt/TiO$_2$-2, and Pt/TiO$_2$-3 materials (**Figure 1A-C**, respectively) indicate the efficient deposition of Pt NPs at the TiO$_2$ supports displaying a uniform surface dispersion, spherical shape, and uniform sizes. The Pt content, as well as Pt NPs size and coverage at the TiO$_2$ surface, could be controlled and increased by performing sequential reduction steps. The ICP-OES analyses indicated the presence of 20.1, 31.0, and 38.4 wt.% of Pt in the Pt/TiO$_2$-1, Pt/TiO$_2$-2, and Pt/TiO$_2$-3 samples, respectively. Moreover, Pt NPs diameters calculated from the SEM images corresponded to 12.2 ± 2.0, 16.0 ± 1.5, and 20.4 ± 2.1 nm, respectively. HRTEM images for the Pt/TiO$_2$-1, Pt/TiO$_2$-2, and Pt/TiO$_2$-3 samples (**Figure 1D-F**, respectively) revealed that the individual Pt NPs were comprised of aggregates made up of individual Pt clusters measuring about 3 nm in size (estimated based on TEM images). While a lower Pt coverage at the TiO$_2$ surface can be observed for both Pt/TiO$_2$-1 and Pt/TiO$_2$-2 samples (**Figure 1D** and **E**), the highest coverage was detected in the Pt/TiO$_2$-3 material (**Figure 1F**). It is highly anticipated that the Pt morphology composed of individual aggregates could lead to high electrocatalytic activities and that their size as well as Pt surface coverage should strongly influence their performances.

After the syntheses, the samples Pt/TiO$_2$-1, Pt/TiO$_2$-2, and Pt/TiO$_2$-3 were incorporated on Vulcan XC-72 Carbon (Cabot®) by wet impregnation. This led to Pt/TiO$_2$-1/C, Pt/TiO$_2$-2/C, and Pt/TiO$_2$-3/C materials, respectively. In all cases, the Pt/TiO$_2$ loading

corresponded to 10 wt.%, reaching the overall Pt loading of 2.01, 3.10, and 3.84 wt.% for

Pt/TiO$_2$-1/C, Pt/TiO$_2$-2/C, and Pt/TiO$_2$-3/C, respectively. **Figure S3** shows the XRD profiles for

the Pt/TiO$_2$-1/C, Pt/TiO$_2$-2/C, and Pt/TiO$_2$-3/C materials. The diffractograms show the

characteristic reflections assigned to TiO$_2$ anatase, *fcc* Pt, and carbon. This indicates that our

wet impregnation approach was effective for the incorporation of TiO$_2$ onto the carbon

support.

Figure 2A-D show the Ti 2p, Pt 4f, C 1s, and O 1s core level XPS spectra along with

their fitting and deconvoluted curves, obtained for the Pt/TiO$_2$-1/C, Pt/TiO$_2$-2/C, and Pt/TiO$_2$-

3/C materials and Vulcan XC-72 Carbon. The corresponding XPS parameters obtained from

the spectra are shown in **Table 1** (for Ti, Pt, and O) and **2** (for C). The Ti 2p spectrum (**Figure**

2A) displayed doublet peaks at 459.4 eV and 465.1 eV assigned to Ti 2p$_{3/2}$ and Ti 2p$_{1/2}$,

respectively. The splitting width between the two peaks was 5.7 eV, indicating the presence

of only the Ti^{4+} chemical state[51]. Ti 2p peaks were slightly shifted towards higher binding

energies as compared to those in TiO$_2$, which indicates a change in the Ti chemical

environment possibly due to strong interactions with the support (such as the formation of

Ti-O-C bonds)[52].

As shown in **Figure 2B**, the Pt 4f region revealed that the 4f$_{7/2}$ and 4f$_{5/2}$ spin-orbital

components had an asymmetric shape which is typical for Pt^0[53,54]. The peaks located at 71.5

and 74.9 eV can be assigned to Pt 4f$_{7/2}$ and Pt 4f$_{5/2}$ of Pt^0, respectively. According to the

literature[54,55], the binding energy value of Pt^0 is located around 71.0 eV. The slight shift

towards higher binding energy values detected herein is attributed to the strong metal-

support interaction and to the Pt nanoparticles sizes (Pt clusters that make up each

nanoparticle). Interestingly, this positive shift also suggests that the interaction between Pt and TiO_2 modifies the electronic properties of Pt by increasing the d-vacancy at the Pt valence bond (5d orbital, Pt d-band donation to Lewis acid centers such as Ti^{x+} at the Pt/TiO2 interface), leading to the electrochemical activation of both TiO_2 and Pt[26,36,56].

Regarding the C 1s region, it was possible to deconvolute the C 1s spectrum into six peaks (**Figure 2C**). The lowest binding energy and dominant peak at about 284.5 eV corresponds to the graphitic carbon phase[57], while the peak at around 286.0 eV is assigned to hydrocarbons (C-H) from defects on the graphitic structure[58]. Three carbon-oxygen bonding structures for the –C-OH, >C=O and –COOH can also be observed at approximately 287.5, 289.2 and 290.8 eV, respectively. The subpeak located at higher than 292.8 eV is related to π → $\pi*$ plasmonic excitation[59]. Since acidic oxygenated species are known to be responsible for the generation of H_2O_2 in the ORR[60,61]. In our case, the Pt/TiO₂-2/C sample presented the lowest amount of oxygenated species on the surface (as seen on I_{oxy}/I_c). This material would thus generate the lowest amount of H_2O_2 during the reaction[50], and hence lead to a higher ORR current density. The O 1s core electrons peaks for the Pt/TiO₂/C electrocatalysts are shown in **Figure 3D**. The O 1s peaks could be deconvoluted in three peaks. According to the literature[52,62], the first component (O_I) centered at 531 eV was attributed to the lattice oxygen in the oxides and C=O functional groups. The second and dominant component (O_{II}) located at 533 eV was attributed to chemisorbed oxygen species (*e.g.*, OH⁻) and functional C-O groups. The last component (O_{III}) with BE around 536 eV were characteristic of adsorbed water.

In the next step, CO stripping was employed to estimate the electroactive area of each material as described in **Figure S4**. The Pt/TiO₂/C materials presented lower onset

potential for carbon monoxide oxidation when compared to commercial Pt/C E-TEK, a behavior related to the Pt and TiO_2 interaction. This interaction modifies the Pt electronic density and decreases the adsorption of CO on a metal surface, facilitating the oxidation process. This effect also was studied by Lewera et al.[63]. and agrees with the binding energy shifts detected in our XPS analyses (**Figure 2**). A main current density peak was detected between 0.76 and 0.80 V *vs* RHE (Reversible Hydrogen Electrode) for all materials, which is assigned to the CO oxidation on the Pt sites interacting with sp^3 disordered carbon[1,64]. In addition, a shoulder at lower potentials was observed (0.46 V *vs* RHE) for the hybrid Pt/TiO_2-3/C electrocatalyst, which can be assigned to the partial agglomeration of Pt nanoparticles on the TiO_2 surface and the increase of the particle cluster size due to the higher Pt coverage in this material. This peak is considered as the main peak on unsupported Pt nanoparticles, therefore, it would suggest that due to its high surface coverage, the Pt/TiO_2-3/C material presents a larger similarity to unsupported Pt NPs[65]. This agrees with SEM and HRTEM images (**Figure 1**)[1]. The ESA (electrochemical surface area) and ECSA (electrochemical active surface area) of the materials calculated from these experiments are depicted in **Table S1**, which also presents the Pt loading on the electrodes[66]. It can be observed that the ECSA increased with the Pt loadings, corresponding to 2.14, 9.78, and 25.2 m^2g^{-1} for Pt/TiO_2-1/C, Pt/TiO_2-2/C, and Pt/TiO_2-3/C materials, respectively. However, it is important to note that these ECSA values were lower as compared to Pt/C E-TEK (68.2 m^2g^{-1}). This is probably due to the aggregation of smaller Pt particles on TiO_2 as observed by HRTEM.

Figure 3A-D depicts the linear sweep voltammetries (LSV) for the Pt/TiO_2-1/C (**Figure 3A**), Pt/TiO_2-2/C (**Figure 3B**), and Pt/TiO_2-3/C (**Figure 3C**) and Pt/C E-TEK (**Figure 3D**) materials

towards the ORR performed in O_2 saturated H_2SO_4 (0.5 mol L^{-1}) at different rotation rates (from 100 rpm to 2500 rpm as indicated by the colors in the inset, **Figure 3A**). The detected currents were normalized by the geometric surface areas of the electrodes (0.2475 cm² for the disk and 0.1866 cm² for the ring) and presented as current densities. **Figure 3E-H** and **I-L** depict the disk currents and Koutechy-Levich plots for ORR, respectively, using each electrocatalyst shown in **Figure 3A-D**. These results show an increase in ring current density values (**Figure 3A-D**) on potentials lower than 0.81 V *vs* RHE, which indicates the conversion of O_2 onto H_2O_2, detected by its oxidation on the ring. The values obtained for our materials, as well as for the commercial one, are in clear agreement with the literature, using the same mass of Pt and same medium as in the present work[21,67–69]. On the other hand, the disk current density (**Figure 3E-H**) is lowered in potentials below 0.81 V, which indicates the formation of H_2O. It is important to note that the current density scale in the ring is on $\mu A\ cm^{-2}$ while on the disk the current density was in $mA\ cm^{-2}$, indicating that water is produced as the main product.

Additionally, LSV of the oxygen reduction on the disk indicate a mixed kinetic – diffusion control region between potentials of 0.91 V and 0.61 V (*vs* RHE). This region is narrower under low rotations and becomes larger at higher rotations. The region between 0.61 V and lower potentials is assigned to the diffusional control region. This behavior is normally seen for Pt-based electrocatalysts[70]. The disk's limiting current density increased gradually with the rotation rate, as expected for a diffusional controlled reaction[71]. The Koutecky-Levich plots (**Figure 3I-L**) was employed to give us an idea about the number electrons involved in the reaction on the disk during ORR for each electrode and the

preferential mechanism. This could be correlated to the oxygen reduction current density with the rotation rate at several potentials according to **Equation 1**:

$$\frac{1}{j} = \frac{1}{j_k} + \frac{1}{j_d} = \frac{1}{j_k} + \frac{1}{B\omega^{1/2}} \tag{1}$$

where B stands for the inverse of the K-L slope between $1/j$ and $1/\omega^2$ defined by *$0.62nFC_{O2}D_{O2}{}^{2/3}v^{-1/6}$*. 0.62 is a constant used when ω (rotating speed) is expressed in rpm, *n* is the number of exchanged electrons, *F* is the Faraday constant (96485 C mol^{-1}), *C_{O2}* is the concentration of dissolved (saturated) oxygen (1.13 × 10^{-6} mol cm^{-3}), *D_{O2}* is the diffusion coefficient of oxygen in the electrolyte (1.8 × 10^{-5} cm^2 s^{-1}) and *v* is the electrolyte kinematic viscosity (0.01 cm^2 s^{-1})[72].

Considering Pt as the standard electrocatalytic metal for ORR via 4 electrons and that the experimental values obtained for Pt/C E-TEK were close to the theoretical ones (slope ≈ 8), the K-L slopes were compared in the mixed diffusion-kinetic control potentials. These values lower when the Pt loading on TiO_2 increases, which could be assigned to the preferential 4-electron mechanism of platinum for ORR. Additionally, the water production efficiency (and consequently, the number of exchanged electrons per O_2 molecule) was calculated using the ring current densities applying the *Jakobs'* method using **Equation 2** and **3**[18]:

$$p\,(H_2O) = \frac{N\left(-\frac{j_D}{j_R} - j_R^0\right) - 1}{N\left(-\frac{j_D}{j_R} - j_R^0\right) + 1} \tag{2}$$

$$n = 2[p(H_2O) + 1] \tag{3}$$

where N is the collection factor (experimentally defined as N= 0.28), j_D is the disk current density, j_R is the ring limiting current density at disk potentials (E_D) lower than 0.91 V (*vs* RHE) and $j_R{}^0$ is the ring limiting current density for disk potentials higher than 0.91 V (*vs*

RHE). These values are listed in **Table 3**. A small amount of electrogenerated hydrogen peroxide is observed from the ring current densities presented in **Figure 3**. When comparing the limiting current densities of the ring and disk on the commercial material, we can see that the ring current density is about 2500 times lower than the disk, confirming that these electrodes produce mainly water (low hydrogen peroxide current). Hence, the number of electrons is closer to 4.

From the ring curves (**Figure 3E-H**), two behavior changes are also noticed at 0.71 V and 0.31 V (*vs* RHE), which were more significantly seen on the Pt/TiO_2-1/C material. It is suggested that the ORR on the disk, and consequently the oxidation of hydrogen peroxide on the ring, occur as a function of the applied potential. Our results suggest that there are probably two mechanisms of formation of hydrogen peroxide, one at lower overpotentials and one at higher overpotentials. This behavior is also observed for other Pt-based materials[70]. In order to better understand the reaction mechanism, Tafel curves were plotted from RDE data by the mass-transport correction of the current density measured for rotating disk electrodes and are presented in **Figure 4** according to **Equation 4**:

$$j_k = \frac{j_d * j}{j_d - j}$$
(4)

where j is the experimentally measured current density, j_d is the obtained diffusion-limited current density, and j_k is the kinetic current density without the mass-transport effect. These values were calculated using the current density normalized by geometric area. The Tafel curves for the electrocatalysts presented two different regions, a behavior which is expected for Pt-based catalysts. At lower overpotentials, all the electrocatalysts presented slopes between -60 and -80 mV dec^{-1} which indicates that the mechanism of oxygen

adsorption is similar to bulk Pt at 1.06 - 0.96 V (*vs* RHE) potentials[32,33,44]. However, at higher overpotentials, there is an increase on the slope with the decrease of the Pt amount on the electrocatalyst[73], from -120 mV dec^{-1} (Pt/C E-TEK) to -266 mV dec^{-1} (Pt/TiO$_2$-1/C). This observation indicates that the current densities are related to the oxygen adsorption energy on the electrocatalyst surface and that the first electron transfer is the determining step of the ORR[35]. These slope values were also observed for other TiO$_2$-based electrocatalysts[32,35,73].

Previous studies have shown that high slopes on the Tafel plot are normally associated with the rate determining step of the ORR, the O$_2$ adsorption onto the metal (M)[74]. Tafel slopes normally increase on materials with lower Pt contents, which indicates that the mechanism tends to involve a 2-electron reaction. This was also observed for our materials when compared to the commercial Pt/C[75]. According to Shinagawa *et al.*[74], the mechanism of the ORR is based on three different surface covering species, which are responsible for the slopes on the Tafel plot. At lower overpotentials, the theoretical slopes can vary from 40 to 120 mV dec^{-1} depending on the adsorbed species contributing to the rate determining step. As the slope lowers, it indicates there are more MOO$^-$ and MOOH species contributing to the rate determining step of the reaction, while at higher slopes the rate determining step is governed by MOO adsorption. Hence, while the reaction on the Pt/C E-TEK catalyst is determined initially by MOO groups, our catalysts depended also on the generation of MOO$^-$ and MOOH groups. On the other hand, at higher overpotentials, the Tafel slope is normally ≥ 120 mV dec^{-1}, which indicates that the MOO and MOOH species are converting into MOO$^-$ species. Thus, higher slopes show that the conversion starts in lower overpotentials or these catalysts already present a high number of MOO$^-$ species on their surface. Moreover, based

on DFT simulations[76], a strong interaction between Pt and TiO_2 is presumed due to the overlapping of the TiO_2 bonding orbitals with the Pt d-orbital. These calculations also indicate a strong interaction between Ti and Pt that could result in a negative overall net charge in this structure which could strengthen the $Pt-O_{ads}$ bond. Therefore, the desorption process could become slow in the high overpotential region, thus increasing the Tafel plot as observed in our results.

In order to better compare the relative ORR electrocatalytic activity of our materials, the ORR linear scanning voltammetries of all our electrocatalysts, at 1600 rpm rotation rate, were plotted as shown in **Figure 5A.** In addition, the electrocatalytic activity normalized by geometric mass (left hand side) and Pt mass on the electrode (right hand side) at 0.90 V (*vs* RHE) is plotted in **Figure 5B**. The Pt/C E-TEK material presented a more positive onset potential for ORR (0.89 V) than the other materials, followed by Pt/TiO_2-2/C (0.88 V), Pt/TiO_2-3/C (0.84 V), and Pt/TiO_2-1/C (0.82 V) which have less than half Pt content in their composition compared to the commercial electrocatalyst. In agreement with the ORR onset potential, the number of transferred electrons follows the pattern Pt/C E-TEK > Pt/TiO_2-2/C > Pt/TiO_2-3/C > Pt/TiO_2-1/C (determined from their K-L plot), indicating that the reaction is kinetically favorable in this same order.

Interestingly, even though the electrodes covered by Pt/TiO_2/C hybrids have Pt loadings that are from 3 to 5 folds lower than the one containing Pt/C E-TEK, they still present similar limiting diffusional current densities[77]. This led to much higher activities when the data is normalized by Pt mass in **Figure 5B**. Specifically, the Pt/TiO_2-2/C material displayed a starting reduction potential close to Pt/C E-TEK (0.89 V and 0.88 V *vs* RHE, respectively). The

higher activity of the Pt/TiO$_2$-2/C material could be attributed to its lowest number of acidic oxygenated species on the surface which lowers the H$_2$O$_2$ formation, thus enhancing the water production and increasing the current on the disk relative to the other materials[50]. This material also displays less Pt aggregation at the surface as compared to Pt/TiO$_2$-3/C (**Figure 1**). It is noteworthy that the Pt/TiO$_2$-1/C sample presented the highest H$_2$O$_2$ production, which can also be attributed to the higher exposure of anatase TiO$_2$ at the surface[34,50]. Since anatase contributes to peroxide generation and our colloidal spheres are mostly composed of anatase TiO$_2$.

As shown by our XPS data (**Figure 2, Table 1** and **2**), the carbon percentage increased in the following order: Pt/TiO$_2$-1/C < Pt/TiO$_2$-2/C < Pt/TiO$_2$-3/C. Even though it could be expected of the third sample to have a higher activity based on the presence of adsorbed oxygenated species, the binding energy of these species is the highest. A higher binding energy indicates a stronger interaction between oxygenated species and the catalyst's surface. In order to increase the reaction rate, these bonds must be weakened, thus allowing a quicker desorption of oxygenated species from the catalyst[78]. This leads to a lower activity on the Pt/TiO$_2$-3/C[14,79]. These results indicate that the control over the Pt NPs size and coverage at the TiO$_2$ surface significantly influences their physicochemical properties and electrocatalytic activities towards the ORR. In this case, rather than an increase in activity with the Pt loading in the materials, a volcano-type relationship was observed, in which the sample produced by two Pt deposition steps (Pt/TiO$_2$-2/C) displayed the highest activities due to the equilibrium between surface coverage and Pt loading. These properties were determining factors to the composition of surface species, which directly influenced the reaction outcome.

We also evaluated the stability of the Pt/TiO$_2$-2/C material relative to Pt/C E-TEK by performing accelerated stress tests (AST) as shown in **Figure 6**. The initial and final ORR polarization curves are depicted as solid and dashed traces, respectively, in **Figure 6A**. The AST curves for the Pt/C E-TEK and Pt/TiO$_2$-2/C are shown in black and red, respectively. It can be observed that a decrease in activity was detected for both materials after the tests. However, when comparing their half-wave potential before and after the AST, E$_{1/2}$, (**Figure 6B)**, a more significant decrease is detected for Pt/C E-TEK, from 0.747 to 0.646 V *vs* RHE compared to Pt/TiO$_2$-2/C, from 0.727 to 0.697 V *vs* RHE. When comparing half-wave potentials, shifts to smaller regions indicate an activity loss, thus, since for the commercial materials the shift is higher (approximately 0.31 V *vs* RHE) when compared to Pt/TiO$_2$-2/C (approximately 0.24 V *vs* RHE), it clearly shows the commercial material is less stable than the synthesized one. This could be explained by the lower degradation of the carbon support by Pt when attached to corrosion-resistant supports such as TiO$_2$[32]. Moreover, after the ATS the number of electrons involved in the reactions and water percentages lowered for both materials, as seen in **Table S2** as estimated by *Jakobs'* method. While the mean electron number was of 3.93 and 3.97 on the TiO$_2$ containing material and commercial material, respectively, they produced 96.5 and 98.4% of water, respectively. This further shows the low loss of overall activity of our material compared to the commercial material.

In addition to metal-support interactions, the utilization of TiO$_2$ as support also enables the harvesting of its photocatalytic properties to further improve activities. Therefore, the influence of UV irradiation on the electrocatalytic activity of the Pt/TiO$_2$-2/C electrocatalyst was also evaluated. In this case, we were interested in investigating to what

extent the UV-light excitation can lead to an increase in activities. The effect of light irradiation was probed in chronoamperometry experiments performed at 0.51 V (*vs* RHE) as shown in **Figure S5A** and the activity towards the ORR by linear scanning voltammogram as shown in **Figure S5B** (rotation rate of 1600 rpm in O_2 saturated 0.5 mol L^{-1} H_2SO_4 solution). Here, the activity under UV excitation was compared with its activity in the absence of UV excitation. **Figure S5A** shows a chronoamperometric assay while applying to the electrode UV light pulses of about 150 seconds. It was observed that under UV light excitation the current density increased in about 4 mA cm^{-2} due to the light excitation. The voltammograms on **Figure S5B** revealed a slight shift to more positive potentials (~30 mV) and an increase of 11.3% on the limiting diffusion current density under UV-excitation. This indicates that the utilization that TiO_2 based electrocatalysts and UV light excitation can be employed to further improve the electrocatalytic activities towards the ORR. It is anticipated that further optimizations can lead to further improvements both in the photoelectrocatalytic activities and in the use of visible light (instead of UV) by TiO_2 doping or use Au NPs (harvesting plasmonic effects).

Conclusions

We unraveled herein how morphological features of hybrids materials comprised of Pt NPs supported on TiO_2 colloidal spheres (Pt/TiO_2) influence their electrocatalytic activities towards the ORR. To this end, it was demonstrated that employing TiO_2 colloidal spheres as physical templates, the uniform deposition of monodisperse and spherical Pt clusters

comprised smaller Pt NPs (~3 nm in size) could be achieved. In this case, both the size of the clusters and the Pt coverage could be tuned as a function of the deposition steps. After incorporating the Pt/TiO_2 materials into Vulcan XC72 Carbon (to produce $Pt/TiO_2/C$ materials), the electrocatalytic activities towards the ORR, the reaction, and enhancement mechanisms were investigated. Our results demonstrated that the control over the Pt coverage at the surface plays a pivotal role over the optimization of activities, in which a relationship between Pt content at the TiO_2 surface and ORR activity was established. More specifically, the material produced from two Pt deposition steps displayed the higher activity as compared with the materials produces after one or three deposition steps. The ORR activity and stability were also superior as compared to commercial Pt/C E-TEK, even at lower Pt loadings (between 2.0 and 4.0 wt.% of Pt on the final material). The variations in catalytic activity could be correlated with the presence and concentration of surface reactive groups, such as adsorbed oxygenated species with lower binding energies, as a function of composition. These species are responsible for the highest current density and low generation of H_2O_2 during the ORR. Moreover, our material contains TiO_2, which aside from increasing the materials stability, also allows a further activity enhancement through UV-excitation. These results illustrate that the understanding of the electrocatalytic enhancement mechanism together with the controlled synthesis of Pt-based nanomaterials can strongly lead to tailored surface properties and thus electrocatalytic activities. We believe the data presented herein shed new mechanistic insights and fundamental understating on the optimization of ORR activities via controlled synthesis and may inspire the development of catalysts displaying improved performances.

.

Acknowledgments

References

1   L. A. Estudillo-Wong, Y. Luo, J. A. Díaz-Real and N. Alonso-Vante, *Appl. Catal. B Environ.*, 2016, **187**, 291–300.

2   A. Holewinski and S. Linic, *J. Electrochem. Soc.*, 2012, **159**, H864–H870.

3   R. Zhou, Y. Zheng, M. Jaroniec and S.-Z. Qiao, *ACS Catal.*, 2016, **6**, 4720–4728.

4   G.-L. Chai, M. Boero, Z. Hou, K. Terakura and W. Cheng, *ACS Catal.*, 2017, acscatal.7b02548.

5   J. Snyder, K. Livi and J. Erlebacher, *Adv. Funct. Mater.*, 2013, **23**, 5494–5501.

6   D. Guo, R. Shibuya, C. Akiba, S. Saji, T. Kondo and J. Nakamura, *Science (80-.).*, 2016, **351**, 361–365.

7   V. R. Stamenkovic, B. Fowler, B. S. Mun, G. Wang, P. N. Ross, C. A. Lucas and N. M.

Markovic, *Science (80-.).*, 2007, **315**, 493–497.

8   J. E. ten Elshof, H. Yuan and P. Gonzalez Rodriguez, *Adv. Energy Mater.*, 2016, **6**, 1600355.

9   Q. Li, R. Cao, J. Cho and G. Wu, *Adv. Energy Mater.*, 2014, **4**, 1301415.

10   Y. Chen, Z. Cai, Y. Kuru, W. Ma, H. L. Tuller and B. Yildiz, *Adv. Energy Mater.*, 2013, **3**, 1221–1229.

11   A. Riese, D. Banham, S. Ye and X. Sun, *J. Electrochem. Soc.*, 2015, **162**, F783–F788.

12   H. Zhang, M. Jin, Y. Xiong, B. Lim and Y. Xia, *Acc. Chem. Res.*, 2013, **46**, 1783–1794.

13   Y. Nie, L. Li and Z. Wei, *Chem. Soc. Rev.*, 2015, **44**, 2168–2201.

14   V. Tripković, E. Skúlason, S. Siahrostami, J. K. Nørskov and J. Rossmeisl, *Electrochim. Acta*, 2010, **55**, 7975–7981.

15   H. S. Casalongue, S. Kaya, V. Viswanathan, D. J. Miller, D. Friebel, H. A. Hansen, J. K. Nørskov, A. Nilsson and H. Ogasawara, *Nat. Commun.*, , DOI:10.1038/ncomms3817.

16   H. Mistry, A. S. Varela, S. Kühl, P. Strasser and B. R. Cuenya, *Nat. Rev. Mater.*, 2016, 16009.

17   S. E. F. Kleijn, S. C. S. Lai, M. T. M. Koper and P. R. Unwin, *Angew. Chemie - Int. Ed.*, 2014, **53**, 3558–3586.

18   L. Demarconnay, C. Coutanceau and J. M. Léger, *Electrochim. Acta*, 2004, **49**, 4513–4521.

19   X. Cheng, Y. Li, L. Zheng, Y. Yan, Y. Zhang, G. Chen, S. Sun and J. Zhang, *Energy Environ. Sci.*, 2017, **10**, 2450–2458.

20   M. Shao, Q. Chang, J.-P. Dodelet and R. Chenitz, *Chem. Rev.*, 2016, **116**, 3594–3657.

21   Y.-H. Shih, G. V. Sagar and S. D. Lin, *J. Phys. Chem. C*, 2008, **112**, 123–130.

22   X. Wang, S.-I. Choi, L. T. Roling, M. Luo, C. Ma, L. Zhang, M. Chi, J. Liu, Z. Xie, J. a. Herron, M. Mavrikakis and Y. Xia, *Nat. Commun.*, 2015, **6**, 7594.

23   Y. Li, J. L. Hart, M. L. Taheri and J. D. Snyder, *ACS Catal.*, 2017, **7**, 7995–8005.

24   Z. F. Huang, J. Wang, Y. Peng, C. Y. Jung, A. Fisher and X. Wang, *Adv. Energy Mater.*, 2017, **1700544**, 1–21.

25   J. Liu, M. Jiao, L. Lu, H. M. Barkholtz, Y. Li, L. Jiang, Z. Wu, D. J. Liu, L. Zhuang, C. Ma, J. Zeng, B. Zhang, D. Su, P. Song, W. Xing, W. Xu, Y. Wang, Z. Jiang and G. Sun, *Nat. Commun.*, 2017, **8**, 1–9.

26   Y.-H. Qin, Y. Li, R.-L. Lv, T.-L. Wang, W.-G. Wang and C.-W. Wang, *J. Power Sources*, 2015, **278**, 639–644.

27   J. C. Matsubu, S. Zhang, L. DeRita, N. S. Marinkovic, J. G. Chen, G. W. Graham, X. Pan and P. Christopher, *Nat. Chem.*, 2016, **9**, 120–127.

28   M. Xu, S. He, H. Chen, G. Cui, L. Zheng, B. Wang and M. Wei, *ACS Catal.*, 2017, **7**, 7600–7609.

29   M. Cao, Z. Tang, Q. Liu, Y. Xu, M. Chen, H. Lin, Y. Li, E. Gross and Q. Zhang, *Nano Lett.*, 2016, **16**, 5298–5302.

30   M. Cargnello, V. V. T. Doan-Nguyen, T. R. Gordon, R. E. Diaz, E. a. Stach, R. J. Gorte, P. Fornasiero and C. B. Murray, *Science (80-.).*, 2013, **341**, 771–3.

31   A. M. El-Sawy, I. M. Mosa, D. Su, C. J. Guild, S. Khalid, R. Joesten, J. F. Rusling and S. L. Suib, *Adv. Energy Mater.*, 2016, **6**, 1–12.

32   B. Ruiz-Camacho, M. A. Valenzuela, R. G. González-Huerta, K. Suarez-Alcantara, S. E.

Canton and F. Pola-Albores, *Int. J. Hydrogen Energy*, 2013, **38**, 12648–12656.

33   B. Ruiz Camacho, C. Morais, M. A. Valenzuela and N. Alonso-Vante, *Catal. Today*,

2013, **202**, 36–43.

34   S. Shanmugam and A. Gedanken, *Small*, 2007, **3**, 1189–1193.

35   J. H. Kim, G. Kwon, H. Lim, C. Zhu, H. You and Y. T. Kim, *J. Power Sources*, 2016, **320**,

188–195.

36   B. Y. Xia, B. Wang, H. Bin Wu, Z. Liu, X. Wang and X. W. (David) Lou, *J. Mater. Chem.*,

2012, **22**, 16499.

37   X. Zhao, W. Jin, J. Cai, J. Ye, Z. Li, Y. Ma, J. Xie and L. Qi, *Adv. Funct. Mater.*, 2011, **21**,

3554–3563.

38   S. Y. Choi, M. Mamak, N. Coombs, N. Chopra and G. A. Ozin, *Adv. Funct. Mater.*, 2004,

14, 335–344.

39   N. Liu, Y. Zhao, X. Wang, H. Peng and G. Li, *Mater. Lett.*, 2013, **102**–**103**, 53–55.

40   B. Fang, A. Bonakdarpour, K. Reilly, Y. Xing, F. Taghipour and D. P. Wilkinson, *ACS*

Appl. Mater. Interfaces, 2014, **6**, 15488–15498.

41   D. Wen, S. Guo, J. Zhai, L. Deng, W. Ren and S. Dong, *J. Phys. Chem. C*, 2009, **113**,

13023–13028.

42   C. Jia, P. Yang, H.-S. Chen and J. Wang, *CrystEngComm*, 2015, **17**, 2940–2948.

43   S. Beak, D. Jung, K. S. Nahm and P. Kim, *Catal. Letters*, 2010, **134**, 288–294.

44   K. Tiido, N. Alexeyeva, M. Couillard, C. Bock, B. R. MacDougall and K. Tammeveski,

Electrochim. Acta, 2013, **107**, 509–517.

45   T. C. Damato, C. C. S. de Oliveira, R. A. Ando and P. H. C. Camargo, *Langmuir*, 2013,

29, 1642–1649.

46   X. Jiang, T. Herricks and Y. Xia, *Adv. Mater.*, 2003, **15**, 1205–1209.

47   Y. Cheng, J. Guo, X. Liu, A. Sun, G. Xu and P. Cui, *J. Mater. Chem.*, 2011, **21**, 5051.

48   A. B. A. A. Nassr, I. Sinev, W. Grünert and M. Bron, *Appl. Catal. B Environ.*, 2013, **142**–
     143, 849–860.

49   A. Al-Otaify, M. a Leontiadou, F. V. E. dos Reis, T. C. Damato, P. H. C. Camargo and D.
     J. Binks, *Phys. Chem. Chem. Phys.*, 2014, **16**, 14189–94.

50   F. V. E. dos Reis, V. S. Antonin, P. Hammer, M. C. Santos and P. H. C. Camargo, *J.
     Catal.*, 2015, **326**, 100–106.

51   C. Liu, R. Tong, Z. Xu, Q. Kuang, Z. Xie and L. Zheng, *RSC Adv.*, 2016, **6**, 29794–29801.

52   P. Wang, S. Zhan, Y. Xia, S. Ma, Q. Zhou and Y. Li, *Appl. Catal. B Environ.*, 2017, **207**,
     335–346.

53   Z. Lian, W. Wang, G. Li, F. Tian, K. S. Schanze and H. Li, *ACS Appl. Mater. Interfaces*,
     2017, **9**, 16959–16966.

54   C. Dablemont, P. Lang, C. Mangeney, J. Y. Piquemal, V. Petkov, F. Herbst and G. Viau,
     Langmuir, 2008, **24**, 5832–5841.

55   H. Kobayashi, M. Teranishi, R. Negishi, S. ichi Naya and H. Tada, *J. Phys. Chem. Lett.*,
     2016, **7**, 5002–5007.

56   Z. I. Bedolla-Valdez, Y. Verde-Gómez, A. M. Valenzuela-Muñiz, Y. Gochi-Ponce, M. T.
     Oropeza-Guzmán, G. Berhault and G. Alonso-Núñez, *Electrochim. Acta*, 2015, **186**,
     76–84.

57   G. Wu, Y. Hu, Y. Liu, J. Zhao, X. Chen, V. Whoehling, C. Plesse, G. T. M. Nguyen, F.

Vidal and W. Chen, *Nat. Commun.*, 2015, **6**, 7258.

58   J.-H. Zhou, Z.-J. Sui, J. Zhu, P. Li, D. Chen, Y.-C. Dai and W.-K. Yuan, *Carbon N. Y.*, 2007, **45**, 785–796.

59   A. Ganguly, S. Sharma, P. Papakonstantinou and J. Hamilton, *J. Phys. Chem. C*, 2011, **115**, 17009–17019.

60   M. H. M. T. Assumpção, R. F. B. De Souza, D. C. Rascio, J. C. M. Silva, M. L. Calegaro, I. Gaubeur, T. R. L. C. Paixão, P. Hammer, M. R. V Lanza and M. C. Santos, *Carbon N. Y.*, 2011, **49**, 2842–2851.

61   M. H. M. T. Assumpção, A. Moraes, R. F. B. De Souza, M. L. Calegaro, M. R. V. Lanza, E. R. Leite, M. A. L. Cordeiro, P. Hammer and M. C. Santos, *Electrochim. Acta*, 2013, **111**, 339–343.

62   J. R. C. Salgado, V. A. Paganin, E. R. Gonzalez, M. F. Montemor, I. Tacchini, A. Ansón, M. A. Salvador, P. Ferreira, F. M. L. Figueiredo and M. G. S. Ferreira, *Int. J. Hydrogen Energy*, 2013, **38**, 910–920.

63   A. Lewera, L. Timperman, A. Roguska and N. Alonso-Vante, *J. Phys. Chem. C*, 2011, **115**, 20153–20159.

64   J. Ma, A. Habrioux, C. Morais, A. Lewera, W. Vogel, Y. Verde-Gómez, G. Ramos-Sanchez, P. B. Balbuena and N. Alonso-Vante, *ACS Catal.*, 2013, **3**, 1940–1950.

65   A. López-Cudero, J. Solla-Gullón, E. Herrero, A. Aldaz and J. M. Feliu, *J. Electroanal. Chem.*, 2010, **644**, 117–126.

66   Y. Zheng, H. Chen, Y. Dai, N. Zhang, W. Zhao, S. Wang, Y. Lou, Y. Li and Y. Sun, *Electrochim. Acta*, 2015, **178**, 74–79.

67   F. H. B. Lima, W. H. Lizcano-Valbuena, E. Teixeira-Neto, F. C. Nart, E. R. Gonzalez and E. A. Ticianelli, *Electrochim. Acta*, 2006, **52**, 385–393.

68   B. Ruiz-Camacho, O. Martínez-Álvarez, H. H. Rodríguez-Santoyo and V. Granados-Alejo, *J. Electroanal. Chem.*, 2014, **725**, 19–24.

69   G. A. Ferrero, K. Preuss, A. Marinovic, A. B. Jorge, N. Mansor, D. J. L. Brett, A. B. Fuertes, M. Sevilla and M.-M. Titirici, *ACS Nano*, 2016, **10**, 5922–5932.

70   L. G. R. A. Santos, K. S. Freitas and E. A. Ticianelli, *Electrochim. Acta*, 2009, **54**, 5246–5251.

71   L. Demarconnay, C. Coutanceau and J.-M. Léger, *Electrochim. Acta*, 2008, **53**, 3232–3241.

72   Y. Feng, T. He and N. Alonso-Vante, *Electrochim. Acta*, 2009, **54**, 5252–5256.

73   K. Tammeveski, *J. Electrochem. Soc.*, 1999, **146**, 669.

74   T. Shinagawa, A. T. Garcia-Esparza and K. Takanabe, *Sci. Rep.*, 2015, **5**, 1–21.

75   N. R. Elezovic, B. M. Babic, V. R. Radmilovic, L. M. Vracar and N. V. Krstajic, *Electrochim. Acta*, 2011, **56**, 9020–9026.

76   L. Li, Z. Wei, Y. Zhang, X. Qi, M. Xia, J. Zhang, Z. Shao and C. Sun, *Sci. China Ser. B Chem.*, 2009, **52**, 571–578.

77   K. Huang, K. Sasaki, R. R. Adzic and Y. Xing, *J. Mater. Chem.*, 2012, **22**, 16824.

78   S. Liu, M. G. White and P. Liu, *J. Phys. Chem. C*, 2016, **120**, 15288–15298.

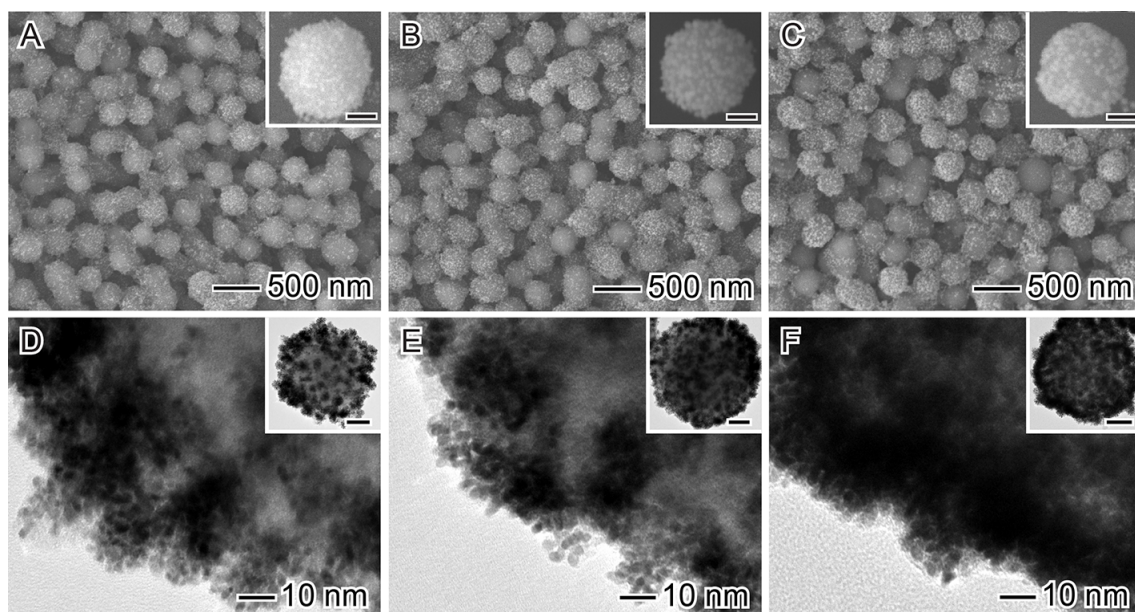79   A. M. Gómez-Marín and J. M. Feliu, *ChemSusChem*, 2013, **6**, 1091–1100.

Figure 1. SEM images of (A) TiO$_2$ colloidal microspheres with supported Pt NPs after one Pt reduction step, (B) two Pt reduction steps, and (C) three Pt reduction steps, and their respective TEM images (D), (E), and (F), respectively. Here, the Pt NPs supported onto TiO$_2$ colloidal spheres grew as clusters of particles after each addition of PtCl$_6^{2-}$, on the sample called Pt/TiO$_2$-1 (A), the apparent sizes seen on SEM were of 12.2 ± 2.0 nm, on Pt/TiO$_2$-2 (B) they measure 16.0 ± 1.5 nm, and on Pt/TiO$_2$-3 (C) they measured 20.4 ± 2.1 nm. Inset bars correspond to 100 nm on (A)-(C), and 50 nm on (D)-(F).
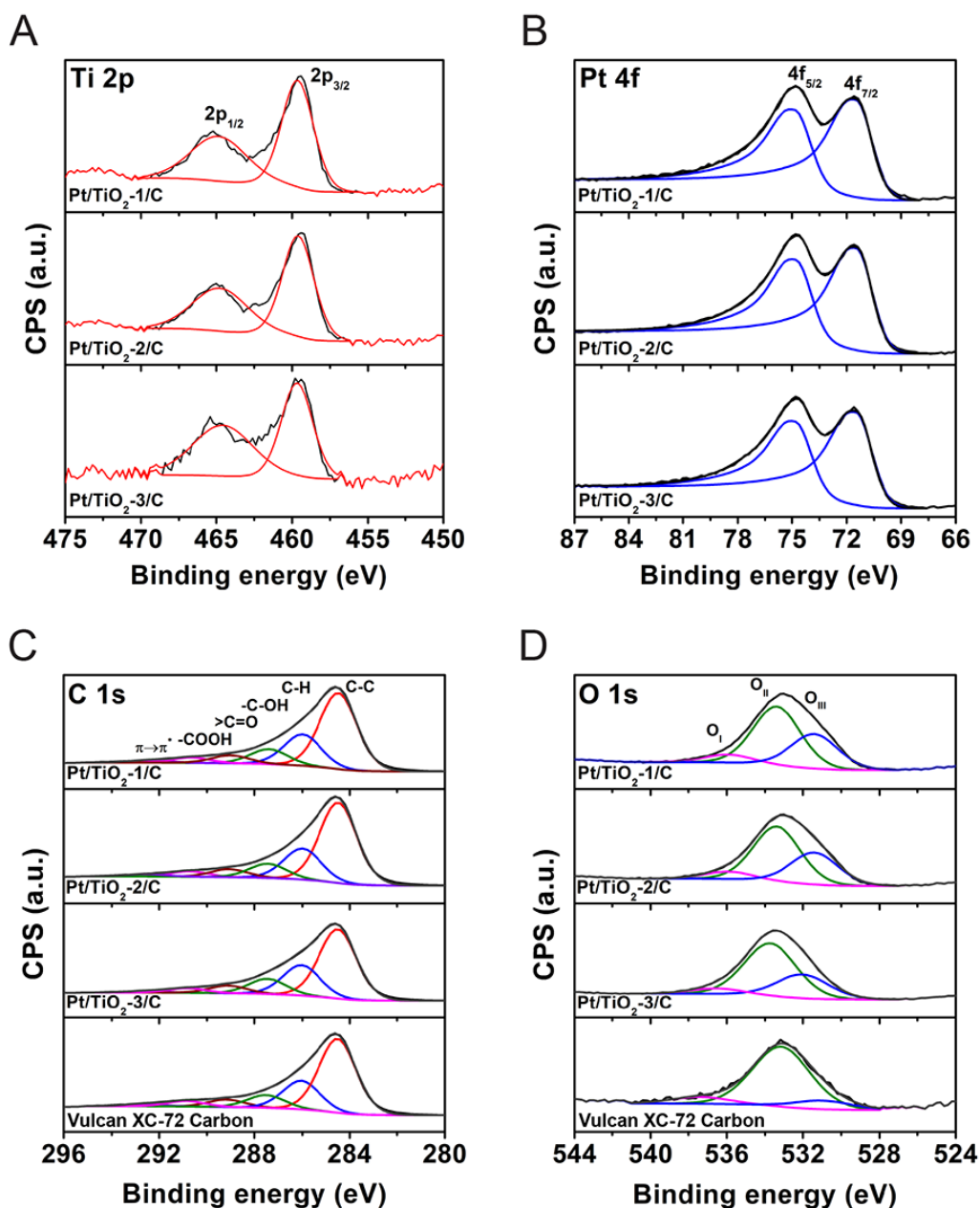
Figure 2. Deconvoluted XPS spectra of Pt/TiO$_2$/C samples and Vulcan XC-72 carbon showing

the binding energy ranges of (A) Titanium 2p, (B) Platinum 4f, (C) Carbon 1s and (D) Oxygen

1s when pertinent. Here, each species in the deconvolution is represented by a different color,

for platinum, platinum (0) is seen in blue, for oxygen, lattice oxygen is seen in blue, surface

oxygen is represented in green, and water oxygen is seen in pink and for carbon, C-C is seen

in red, C-H is represented in blue, C-OH in green, >C=O in brown, COOH in pink and π → π* is
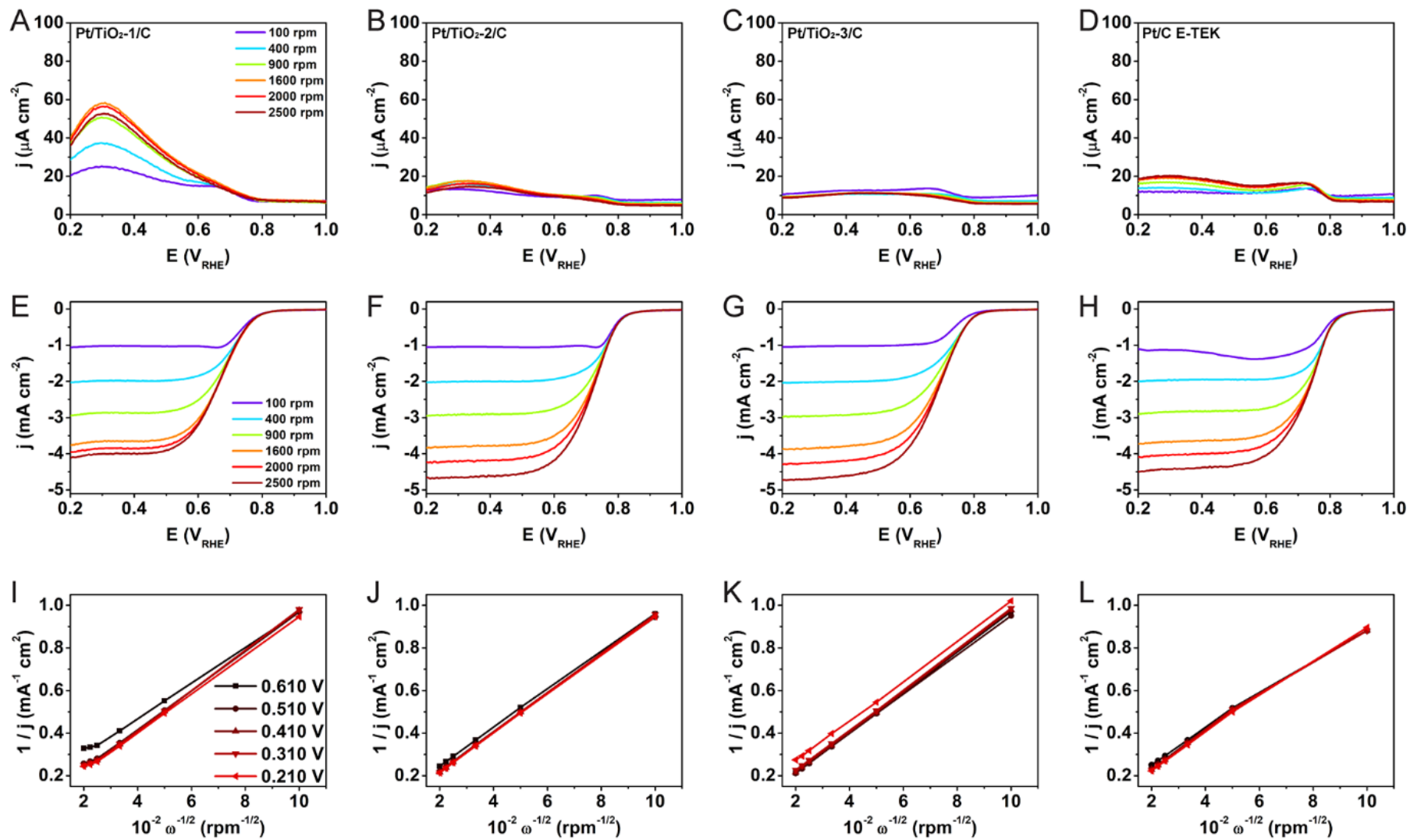
seen in purple.

Figure 3. (A-D) Rotating ring voltammograms for the oxygen reduction reaction on Pt/TiO_2-1/C (A), Pt/TiO_2-2/C (B), Pt/TiO_2-3/C (C), and Pt/C E-TEK (D). These experiments were performed in O_2 saturated 0.5 mol L^{-1} H_2SO_4 with a sweep rate of 10 mVs^{-1} at different rotation rates and 273 K. (E-H) depict the respective rotating disk voltammograms for the samples depicted in (A-D). Each color represents the voltammetric profile obtained when applying their individual rotation rate. (I-L) shows the respective Koutecky – Levich plots for the samples depicted in (E-H).
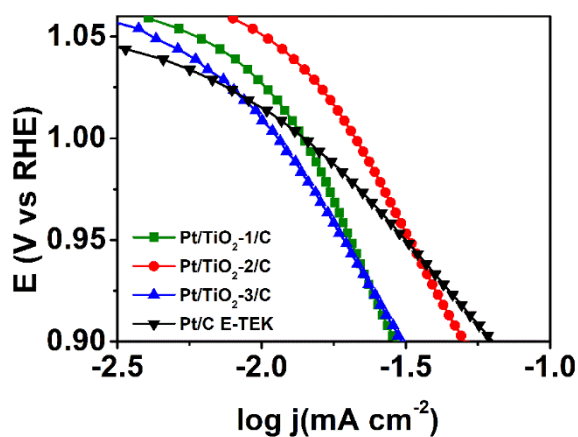
Figure 4. Tafel plots of Pt/TiO$_2$-1/C, in green, Pt/TiO$_2$-2/C, in red, Pt/TiO$_2$-3/C, in blue, and Pt/C E-TEK, in black, normalized by the geometric area of the electrode, data calculated from their corresponding rotating disk electrode data. In these graphs, the data is divided by higher overpotentials and lower overpotentials which leads to information regarding the mechanism of the reaction.
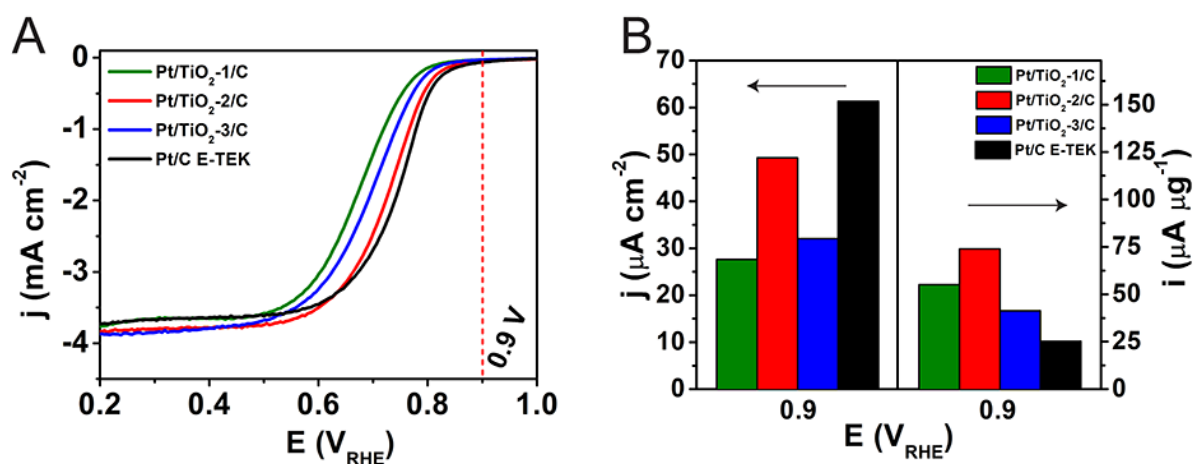
Figure 5. (A) Comparison of rotating disk linear scanning voltammetry for the ORR on Pt/TiO$_2$-1/C, green line, Pt/TiO$_2$-2/C red line, Pt/TiO$_2$-3/C, blue line, and Pt/C E-TEK, black line, in O$_2$ saturated 0.5 mol L^{-1} H$_2$SO$_4$ solution at a rotation rate of 1600 rpm and (B) their respective current densities at a 0.69 V vs Ag/AgCl potential (0.9 vs RHE) on the left hand side of the figure and currents divided by Pt mass in each electrode on the right hand side of the figure. T = 273K.
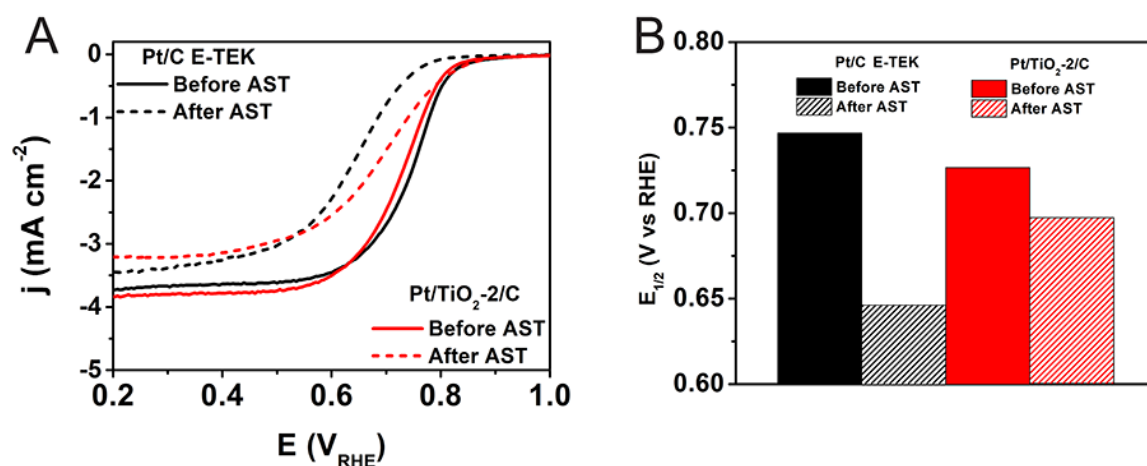
Figure 6. (A) Comparison of ORR polarization curves of Pt/TiO$_2$-2/C, red line, and Pt/C E-TEK, black line, before and after accelerated stress tests, full line and dashed line, respectively. AST were performed using a 100 mV s^{-1} scanning rate and 1000 voltammetric cycles from -0.2 to 0.8 V. ORR was performed in O$_2$ saturated 0.5 mol L^{-1} H$_2$SO$_4$ solution at a rotation rate of 1600 rpm. (B) Half-wave potential for each sample before and after the accelerated stress test. T = 273K.

Table 1 - XPS characteristics of Pt 4f$_{7/2}$, Ti 2p and O 1s region for Pt/TiO$_2$/C samples and Vulcan XC-72 Carbon.

Material	Binding energy (eV)				
	Pt 4f$_{7/2}$	Ti 2p$_{3/2}$	O 1s		
			O$_I$	O$_{II}$	O$_{III}$
Vulcan XC-72	n.d.	n.d.	530.9 (11)*	533.2 (80)	536.8 (9)
Pt/TiO$_2$-1/C	71.5	459.6	531.4 (34)	533.4 (58)	536.0 (8)
Pt/TiO$_2$-2/C	71.5	459.6	531.4 (32)	533.3 (60)	535.9 (8)
Pt/TiO$_2$-3/C	71.5	459.7	531.7 (28)	533.7 (65)	536.5 (7)

*Species percentage

Table 2- XPS characteristics of C 1s region for Pt/TiO$_2$/C samples and Vulcan XC-72.

Material	Binding energy C 1s (eV)						Intensity (%)
	Peak I C-C	Peak II C-H (defects)	Peak III -C-OH	Peak IV >C=O	Peak V - COOH	Peak VI π→π*	I$_{Oxy}$/I$_C$**
Vulcan XC-72	284.5 (57)*	286.0 (21)	287.5 (10)	289.2 (6)	290.8 (4)	292.8 (2)	19
Pt/TiO$_2$-1/C	284.5 (55)	286.0 (23)	287.4 (10)	289.0 (6)	290.6 (4)	292.4 (2)	26
Pt/TiO$_2$-2/C	284.5 (57)	286.0 (22)	287.4 (10)	289.0 (6)	290.8 (4)	292.5 (1)	25
Pt/TiO$_2$-3/C	284.5 (54)	286.0 (24)	287.5 (11)	289.1 (6)	290.8 (4)	292.5 (1)	27

* Species percentage

**Intensity of three oxygen-containing functional groups (peaks III-V) in % of total C 1s area.

Table 3 – Summary of the RDE and RRDE data obtained from oxygen reduction reaction using Pt/TiO$_2$/C and Pt/C E-TEK materials.*

E vs Ag/AgCl	Pt/TiO$_2$-1/C		Pt/TiO$_2$-2/C		Pt/TiO$_2$-3/C	
	nRRDE	p(H2O)%	nRRDE	p(H2O)%	nRRDE	p(H$_2$O)%
0.4	3.95	97.4	3.98	99.2	3.98	99.1
0.3	3.93	96.4	3.98	98.9	3.98	99.2
0.2	3.89	94.4	3.98	98.5	3.97	99.2
0.1	3.85	92.6	3.97	98.3	3.96	99.4
0	3.90	95.0	3.96	98.8	3.97	99.5

* Estimated values using *Jakobs'* method